Asymmetry effects in atomically resolved STM images of Cu(014)-O and W(100)-O surfaces measured with MnNi tips

S. Murphy,[1] K. Radican,[1] I. V. Shvets,[1] A. N. Chaika,[2] V. N. Semenov,[2] S. S. Nazin,[2] and S. I. Bozhko[2,3]
[1]*CRANN, School of Physics, Trinity College, Dublin 2, Ireland*
[2]*Institute of Solid State Physics, RAS, Chernogolovka, Moscow District 142432, Russia*
[3]*NT MDT, Zelenograd, Moscow 124460, Russia*
(Received 24 May 2007; published 19 December 2007)

We report on scanning tunneling microscopy (STM) studies of the Cu(014)-O and W(100)-O surfaces using MnNi tips. The STM data demonstrate asymmetry effects in atomically resolved images of W(100)-O as well as a regular apparent doubling of surface atomic features along the {110} direction in Cu(014)-O surface images. A qualitative explanation of the observed features based on tight-binding (TB) and density functional theory (DFT) calculations of the electronic structure of the MnNi tip is presented. The experimentally observed tip-sample distance dependence of atomically resolved images of Cu(014)-O surface and results of DFT and TB calculations show a significant role of different electron orbitals on both the tip and the surface atoms in the STM image formation.

DOI: 10.1103/PhysRevB.76.245423 PACS number(s): 68.37.Ef, 71.15.Mb, 73.20.At, 73.40.Gk

I. INTRODUCTION

The material of the scanning probe microscopy (SPM) tip and its preparation procedure are the key factors determining the resolution and kind of information included in SPM data. Utilizing a variety of scanning tunneling microscopy (STM) tips provides the possibility of obtaining different information in atomically resolved images.[1–7] In the meantime, the origin of atomic resolution in each particular case still cannot be easily deduced in a straightforward manner despite substantial experimental and theoretical efforts.[8–21] In the early years of STM, the concept of atomic resolution on metals was understood in terms of a single tip orbital of *s*-like character being responsible for the surface images.[8,9] However, this concept was unable to explain tip electronic structure effects reported in the literature for the first time by Tromp *et al.*[10] as well as giant atomic corrugations frequently observed in real experiments on various metal surfaces including close-packed surfaces. Elastic deformation of the tip apex[11–15] and electronic structure effects[17–21] were mainly considered in the literature as two possible mechanisms of corrugation enhancement in STM experiments. One of the explanations of the experimentally observed atomic features with large corrugation heights was given by Chen[18–20] in terms of the actual electronic states on realistic tips. Within this framework, it was shown that the atomic resolution and large corrugations in STM images of metallic surfaces are most probably observed due to d and p_z tip states.[18,19] The tunneling matrix elements for these states are proportional to the z derivative of the surface atom wave function at the center of the tip apex atom.[19] Therefore, it was predicted that the best candidates for STM tips are d-band metals possessing $d_{3z^2-r^2}$ states at the apex atom and semiconductors with p_z dangling bonds. The latter was also proposed from the results of STM experiments on the reconstructed Si(111) surface. It was found that STM tips which picked up a silicon cluster with a single p_z dangling bond at the apex atom produced better contrast in atomically resolved Si(111)-(7×7) images.[16] If tip states with nonzero angular momentum component m along the surface normal dominate near the Fermi level, enhanced but inverted corrugations are predicted by theory.[20] In a more recent coupled tip-surface system analysis,[21] it was also demonstrated that electron states with $m\neq0$ could yield significantly larger corrugation compared to the $m=0$ states. However, the relative contributions of different orbitals can show a rather strong dependence on the tip-surface separation as suggested by some theoretical and experimental studies.[21–25] In most STM experiments, the fine electron structure effects are usually masked because the tunnel current is actually given by a convolution involving different tip and surface states. The effects of the tip electronic structure were recently observed in ultimately high resolution atomic force microscopy experiments on Si(111) and graphite.[26–28] Recent results demonstrate that similar fine effects may play a significant role in dynamic STM experiments on Si(111) where the observed subatomic features could be understood in terms of scattering of electrons into double dangling bonds of the silicon tip atoms.[29] The use of dynamic STM mode for atomic orbital imaging[29,30] was necessary because of the crucial importance of having rather small tip-surface separations (3–5 Å) which could be achieved reproducibly without tip breaking due to lower lateral forces with an oscillating probe.

In this paper, we present high resolution data on Cu(014)-O and W(100)-O surfaces obtained by employing a MnNi probe in STM instruments operated in constant current mode. The rationale for using tips of this material is that the atom at the tip apex could collect electrons via the different $3d$ orbitals. In our studies, we were specifically looking for unusual atomic-scale effects, e.g., asymmetry of atomic features or possible multiple imaging of each atom. We aimed to address the following question: Can an atomically sharp tip behave as a multiple tip with subatomic separation between the tip apexes? The surfaces of Cu(014)-O and W(100)-O were chosen since they are understood by us on the atomic scale,[1,3] and furthermore, they contain both metal and oxygen ions. This is likely to produce a strong electric crystal field at the surface. Hence, placing the apex atom in this

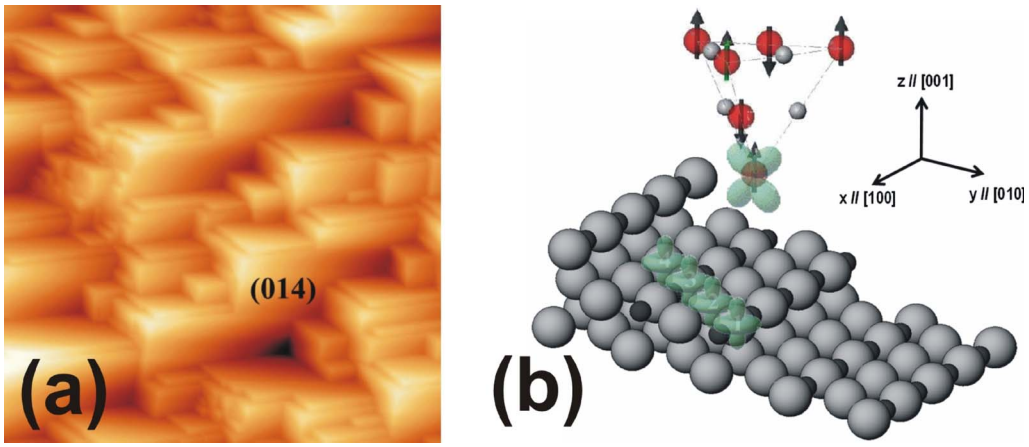

FIG. 1. (Color online) (a) STM image of the faceted Cu(115)-O surface (1×1 μm^2, $V=-800$ mV, and $I=0.12$ nA). (b) Model of the Cu(014)-O surface and MnNi tip. Large gray balls represent Cu atoms, small black balls denote O, red balls for Mn, and small gray balls denote Ni. Arrows indicate the Mn magnetic moment direction. A d_{yz} tip state scanning over $d_{3z^2-r^2}$ surface states can result in doubling of the atomic features in STM images.

crystal field could affect its 3*d* orbitals and this could induce unusual tip effects.

II. EXPERIMENT

The STM studies of the oxygen-induced copper surface reconstruction were carried out in the ultrahigh vacuum chamber of a LAS-3000 (RIBER) spectrometer equipped with Auger electron spectroscopy (AES), low energy electron diffraction (LEED), and room temperature STM (GPI-300). The base pressure in the analytical chamber was less than 1×10^{-10} Torr. For the studies, we used a Cu(115) single crystalline sample with oxygen saturated bulk.[31] The sample preparation procedure has been described in detail earlier.[1] Here, we just mention that the Cu(115) sample was faceted by annealing at temperatures about 600 °C. At this temperature, oxygen outdiffused to the surface and oxygen-driven faceting to {014}-type and (001) planes occurred (Fig. 1). The measured "peak-to-peak" heights in AES spectra give an $I_{O(512)}/I_{Cu(920)}$ ratio of 0.16 ± 0.03 which, according to Ref. 32, corresponds to a half-monolayer oxygen coverage. Atomically resolved STM images of the Cu(014)-O surface were measured on one of the faces of the oxygen-induced reconstructed surface as indicated in Fig. 1(a).

A full description of the preparation of the oxygen-covered W(100) surface is given elsewhere.[33] Briefly, a W(100) surface was cleaned by repeated cycles of oxidation at 1750 K in 10^{-6} Torr O_2 and flash annealing to 2500 K under UHV conditions. The oxidized surface was likewise produced by annealing at 1500 K in 10^{-6} Torr O_2 for several hours, followed by repeated flash annealing to 2300 K in UHV until a sharp $p(3\times1)$ LEED pattern was obtained. STM measurements were carried out in a homebuilt instrument (Trinity College Dublin).

All STM images of both Cu(014)-O and W(100)-O surfaces were measured at room temperature in constant current mode with MnNi probes. Atomically resolved images of W(100)-O reconstruction were typically obtained with $I=0.1$ nA for the tunnel current and a positive sample bias of $V=30$ mV with respect to the tip. The tunneling parameters during the Cu(014)-O surface studies were varied to obtain some information on the STM image formation process.

The MnNi tips were prepared by direct current etching of 0.5 mm diameter polycrystalline rods in a 0.5*M* solution of HCl. The active etching region is physically restricted by covering the lower end of the MnNi rod with a 3–4 mm long section of insulating tubing (e.g., Teflon) before immersion in the etchant.[3] Upon insertion into the UHV system, the tips were subjected to an ion etch with 0.5–1.0 keV Ar^+ ions before being used in the STM. Sometimes, to obtain atomic resolution images of Cu(014)-O surface, a series of bias voltage pulses with amplitudes around 4.0–4.5 V was applied to the tip. This treatment could also be necessary in the cases of occasional tip crashes during scanning.

III. RESULTS AND DISCUSSION

A. Scanning tunneling microscopy studies of oxygen-induced reconstructions

1. Cu(014)-O

As revealed by x-ray diffraction,[34] density functional theory (DFT),[35] and STM[1] data, the Cu(014)-O surface at 0.5 monolayer coverage consists of four-atom wide (001) terraces separated by monatomic steps [Fig. 1(b)] with each (001) terrace containing four copper rows in the [100] direction and with oxygen atoms located between copper atoms in the first and third rows of the terraces. Our previous STM studies of the Cu(014)-O surface using W probes[1] revealed a selective visualization of atomic features governed by the electronic structure of the tip and the surface. As a result, none of the images demonstrated an atomic arrangement, which is in obvious agreement with the overlayer model presented in Fig. 1(b). Usually one, two, or three atomic rows within terraces could be distinguished depending on the scanning parameters and the tip state. In some special cases,

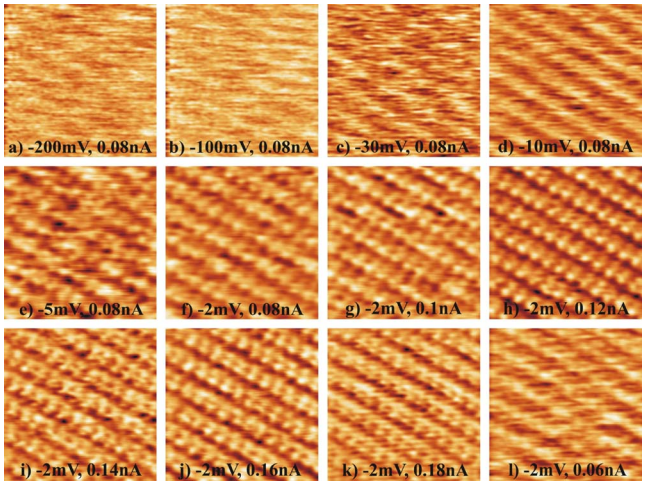

FIG. 2. (Color online) A series of successive 4.5×4.5 nm^2 STM images of the Cu(014)-O surface measured by MnNi probes at different tunneling gap resistances. STM images were plotted using WSXM software (Ref. 38).

four copper atomic rows within terraces could be resolved.[1] As a result, to recover the Cu(014)-O surface atomic structure from the STM images, one needs supplementary information obtained by other techniques,[34,35] detailed theoretical calculations of the surface electronic structure, and a number of STM images which reveal different atomic features within the terraces.[1]

Some of the atomically resolved images of the Cu(014)-O surface are shown in Fig. 2 which presents a series of successive STM images measured with a MnNi probe at different tunneling gap resistances. The set of images reveals that selective imaging of atomic rows within the terraces actually depends on the tip and surface electronic structure as well as on the tip-surface separation. The gap resistance in the course of the measurements was first gradually reduced [from Fig. 2(a) to Fig. 2(k)] and then increased again [Fig. 2(l)] to check the reproducibility of the observed image symmetry change. The key question in these studies is whether it is possible to perform the gap resistance (i.e., tip-sample separation) dependence measurements without modifying the tip because of the tip-surface interaction or tip atom electromigration. Our experimental data[1] show that well resolved images of the Cu(014)-O surface can be obtained at rather small separations that increase the probability to modify the tip during the measurements. This probability also increases with increasing tip load (e.g., simultaneously applying high current and bias voltages). Presumably, for this reason, we could not resolve a reliable gap resistance dependence of the images with unchanged tip at relatively large fixed bias voltages (they demanded larger tunneling currents). At smaller bias voltages of the order of several millivolts, the noise level in the tunnel current channel did not allow atomically resolved imaging of Cu(014)-O surface at currents below 0.04 nA. As a consequence, the sequence of images presented in Fig. 2 is the result of a compromise between the tip load and the possibility of achieving atomic resolution on the Cu(014)-O surface. At the first stage, the bias voltage was decreased from −200 to −2 mV at fixed current of 0.08 nA [Figs. 2(a)–2(f)] and then the tunneling current was increased from 0.08 to 0.18 nA [Figs. 2(f)–2(k)] and reduced again to 0.06 nA [Fig. 2(l)]. To avoid undesirable tip changes, the presented sequence of images was measured as quickly as possible (within 15 min), omitting any time consuming tunneling parameter adjustments during distance dependence measurements. Therefore, the series of consecutive images in Fig. 2 does not demonstrate all possible kinds of Cu(014)-O atomically resolved STM images which could be resolved after fine parameter adjustments.[1] The absence of crashes and reversibility of the image transformations [compare the structure of the images in Figs. 2(d) and 2(l) measured at larger gap resistances] suggest that the tip state was not modified. Thus, the changes observed with decreasing gap resistance can be attributed to the tip-surface distance dependence of the Cu(014)-O images measured with the MnNi tip.

The sequence of atomically resolved STM images reveals a successive change of the image structure: (i) at the largest gap resistances [Figs. 2(a) and 2(b)], only faint traces of the hill and valley structure due to the step periodicity as well as some smaller features can be observed; (ii) at lower gap resistances [Fig. 2(c) and 2(d)], one can resolve a 7.2 Å step periodicity though atomic features within terraces are barely distinguishable; (iii) then, at still lower gap resistances, the images demonstrate one well pronounced atomic row with enhanced corrugations along the steps and less pronounced features between the steps [a representative example is shown in Fig. 2(h)], and (iv) finally, at some tip-surface distance [Fig. 2(j)], we could clearly resolve two atomic rows within the terraces. The images in Figs. 2(i) and 2(k) show some intermediate cases between the images presented in Figs. 2(h) and 2(j). The lower contrast in the image of Fig. 2(k) compared with that in Figs. 2(h) and 2(j) also reveals that at some smaller tip-surface distance, the corrugation heights start to decrease again with decreasing distance. This observation is in qualitative agreement with experimental results obtained on the Cu(100) surface[36] where enhancement of atomic corrugations with decreasing tip-surface distance was changed to reduction at some tip-surface separations. Possible explanations of this attenuation in the small gap resistance range were given in the literature.[14,21] The corrugations could be reduced when the tip atom is very close to the surface atoms because of the apex atom motion[21] or quenching of the surface states[14] due to high electric fields.

The STM images presented in Fig. 2 show some typical examples of selective atom visualization on Cu(014)-O surface arranged in accordance with the overlayer model shown in Fig. 1(b). It is evident that the structure of the obtained atomically resolved images is rather sensitive to both the bias voltage and the tunneling current. The sharp distance dependence of the image structure and atomic corrugation values also suggest that the effects observed take place at rather small tip-surface distances (lower than 5 Å). Similar effects of the gap resistance dependence of the STM images of metal oxide surfaces were recently reported for Ru-O systems.[23,24] STM studies of O/Ru(0001) systems at different bias voltages and tunneling currents[23] unambiguously revealed that the structure of the atomically resolved images of these oxide systems can strongly depend on the tunneling gap resistance due to the dominating contribution of p_z and

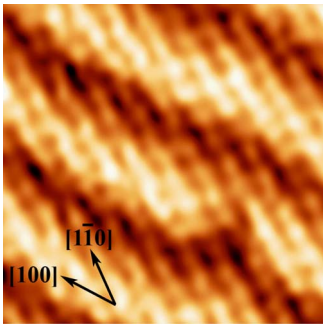

FIG. 3. (Color online) 2.1×2.1 nm^2 STM image of the Cu(014)-O surface demonstrating doubling of the atomic features along the close-packed [1$\bar{1}$0] direction ($V=-30$ mV, $I=0.08$ nA). A single atom defect demonstrates the sharpness of the tip.

$s/p_{x,y}$ orbitals associated with surface atoms at high and low resistances (larger and smaller tip-surface distances), respectively. In the case of the Cu(014)-O surface, we can suggest different partial contributions of Cu $d_{3z^2-r^2}$, d_{xz}, d_{yz}, d_{xy}, $d_{x^2-y^2}$ and O p_z, $p_{x,y}$ orbitals at different tip-surface separations. The change in the partial contribution of different electron states, as well as the relaxation of tip and surface atoms due to the tip-sample interaction, can be considered as possible reasons for the corrugation enhancement in the images shown in panels (g)–(j).

Remarkably, in some cases, STM images of the Cu(014)-O surface demonstrated doubling of the copper atomic features along the close-packed [1$\bar{1}$0] (Fig. 3) or [110] direction. Note that the images shown in Figs. 2 and 3 were measured in different experiments, so that the comparison of bias voltages and tunneling currents cannot provide any reliable information because of different tip states involved in formation of the current. Figure 3 displays a period corresponding to the regular stepped surface terraces of 7.2 ± 0.2 Å width, with step edges directed along the [100] direction and an additional fine structure on the terraces. The terrace structure clearly seen in the image cannot be brought into full agreement with the model presented in Fig. 1(b). We can detect eight maxima per terrace width along the close-packed direction instead of four as expected from the atomic arrangement shown in Fig. 1(b). At the same time, the distance between [1$\bar{1}$0] rows is in agreement with the known lattice parameter. In addition, the image in Fig. 3 displays a single atom defect (i.e., kink site) proving the sharpness of the MnNi tip. The 7.2 Å step periodicity was documented in STM images of Cu(014)-O measured at different bias voltages (from -2 to -800 mV) and tunneling currents (from 0.05 to 0.8 nA). However, the doubling of atomic features along one of the close-packed directions was clearly observed in only some experiments for certain tunneling tip states and scanning parameters. Well resolved images with clearly seen doubling were measured at sample bias voltages between -30 and -50 mV and tunneling currents between 0.05 and 0.08 nA. Our experiments showed that eight features along the [1$\bar{1}$0] direction could be resolved for certain tunneling conditions at different scan rates and fast scan axis directions.[37] The splitting of atomic features along the [110] direction was observed less often than along the [1$\bar{1}$0] one and was not so well resolved. Typically, the images with subtle subatomic structure appeared after a series of bias voltage pulses (4–4.5 V) producing a suitable MnNi apex.

2. W(100)-O

The $p(3\times1)$ W(100)-O surface comprises orthogonal domains of a missing-row reconstruction with either single or double layers of nonmissing W⟨010⟩ rows, which are observed in different domains on the same surface.[33] The boundaries separating these reconstruction domains are decorated by a penetrated oxide WO_x.

During the course of STM measurements performed on the W(100)-O surface with a MnNi tip, several tip changes were encountered as a result of the tip coming into contact with the WO_x-decorated boundaries between the surface domains. In some cases, such as that shown in Fig. 4(a), the tip change produced a modification of the apparent structure in both of the orthogonal domains. This implies that while there is some change in the electronic state at the tip apex, it essentially retains a symmetric character (i.e., a $d_{3z^2-r^2}$ state in the case of a metal apex atom or a p_z state for an adsorbed oxygen atom). However, in other cases, the appearance of only one of the orthogonal structures is modified by a tip change, implying that the tip state switches from symmetric to asymmetric behavior (i.e., to a d_{xz} or d_{yz} state for a metal apex atom or p_x or p_y state for adsorbed oxygen). An example of this effect is shown in Fig. 4(b) which shows a large area scan on which two tip changes are indicated. Figures 4(c) and 4(d) show magnified images of the regions where a tip change results in the modification of the imaged structure in only one of the orthogonal domains. In Fig. 4(c), for example, it can be clearly seen that the tip change results in a modification of the imaged structure of domain A, while that of the orthogonal domain B remains unchanged. In Fig. 4(d), the imaged structure in the corner of domain C is modified, while the orthogonal domain D remains unchanged. In this case, the adjacent domain E, which is aligned parallel to C but is one terrace (i.e., 1.6 ± 0.1 Å) below it, also remains unchanged. This suggests that the tip-surface separation may also be influencing the imaging process.

To obtain the different imaged topology in the orthogonal domains in Figs. 4(c) and 4(d), it is clear that the tip switches reversibly as it scans over the oxide-decorated domain boundary between the domains. Confirmation of this is found by comparing the imaged domain structure on either side of the tip change in Figs. 4(c) and 4(d) in more detail. It can be seen that there is a lateral shift of the rows by half an inter-row spacing (i.e., 1.6 Å). This lateral shift can be associated with the apex atom of the tip hopping by one lattice spacing over the surface of the tip apex. The change in coordination site of the apex atom (as we shall see from the DFT calculations presented later) results in a different tip state being produced at the tip apex. Specifically, the tip state switches reversibly between a symmetric state and an asymmetric state. In the case of the asymmetric state, instead of imaging two W⟨010⟩ rows with equal corrugation, one of the W⟨010⟩ rows appears more prominently than the other. This is illus-

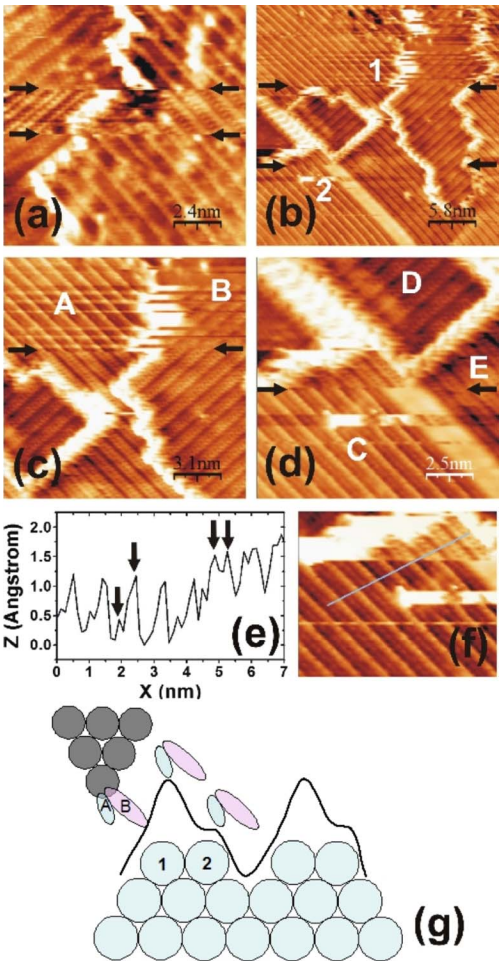

FIG. 4. (Color online) (a) 12×12 nm^2 STM image of two orthogonal domains of the $p(3\times1)$ W(100)-O missing-row reconstruction separated by a WO_x boundary. The positions of two tip changes which modify the apparent structure in both domains are marked with arrows. (b) 29×29 nm^2 STM image of several $p(3\times1)$ W(100)-O domains. Arrows highlight the positions of tip changes, which give rise to changes in the imaged structure of the domains in regions 1 and 2. (c) 15×15 nm^2 zoom in of region 1. The tip change modifies the imaged structure in domain A, but that of the orthogonal domain B remains unchanged. (d) 13×13 nm^2 image of region 2, the structure of domain C is modified, but the orthogonal domain D is unchanged. The parallel domain E, which lies one terrace below C, is also unchanged. (e) Line profile taken across the tip change in the direction marked in (f), showing how two equivalent W⟨010⟩ rows are imaged on the upper side of the tip change, while inequivalent rows are imaged on the lower side. The scan was obtained in the forward-x direction. (g) Schematic model of a tip with two unequal lobes A and B protruding into vacuum, which yields an inequivalent corrugation over rows 1 and 2 of the surface reconstruction. Three different positions of the tip state relative to the surface are shown as the tip moves in the forward-x direction.

trated in the line profile shown in Fig. 4(e), which was taken across the tip change in direction indicated in Fig. 4(f). It should be noted that a double tip effect can be excluded as the source of the line profile in Fig. 4(e). The nearest-neighbor separation on the W(100)-O surface (3.2 Å) is

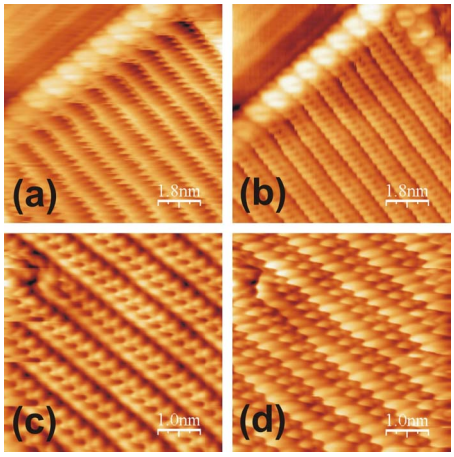

FIG. 5. (Color online) [(a) and (b)] 9×9 nm^2 STM image of two orthogonal $p(3\times1)$ W(100)-O domains scanned in (a) the x direction and (b) the y direction. [(c) and (d)] 5×5 nm^2 STM image of a $p(3\times1)$ W(100)-O domain scanned in the (c) forward-x and (d) reverse-x directions. All images were taken with the same MnNi tip and $I=0.1$ nA and $V=30$ mV.

much larger than that on the MnNi(111) surface ($\leqslant$2.6 Å), meaning that a double tip effect would be apparent regardless of whether the tip scans parallel or perpendicular to the nonmissing W⟨010⟩ rows. Therefore, both orthogonal domains in Figs. 4(c) and 4(d) would be modified. Imaging W⟨010⟩ rows with different corrugations might instead be possible with a single atom tip state similar to that shown schematically in Fig. 4(g). The tip has two unequal lobes (A and B) which protrude into vacuum. The model shows the position of the tip in three different positions relative to the surface. In the first position, lobe A samples the first nonmissing W⟨010⟩ row. In the second position, both lobes contribute to the tunnel current, so that the imaged corrugation is enhanced. In the third position, lobe A samples the second nonmissing W⟨010⟩ row, while lobe B is located over the position of the missing row, so that the corrugation is reduced.

Further evidence of an asymmetric tip state was observed as a sensitivity of the imaged topography with respect to the scan direction. Figures 5(a) and 5(b) show the same area between two domains scanned in the x and y directions, respectively, with the same speed and feedback parameters. The appearance of the larger domain in the image changes substantially with the scan direction, while the appearance of the orthogonal domain in the upper left corner of each image remains the same in both directions. Figures 5(c) and 5(d) show another example of an area scanned this time in the forward-x and reverse-x directions using identical speeds and feedback control, which display substantially different structures. All four images in Fig. 5 were taken with the same tunnel parameters ($I=0.1$ nA and $V=30$ mV).

To clarify possible reasons for the appearance of such unusual STM images of the Cu(014)-O and W(100)-O surfaces, we performed calculations of the MnNi tip electronic structure using both tight-binding (TB) and DFT approaches. For qualitative explanation of the tip-surface distance dependence of the Cu(014)-O STM images with selective atom

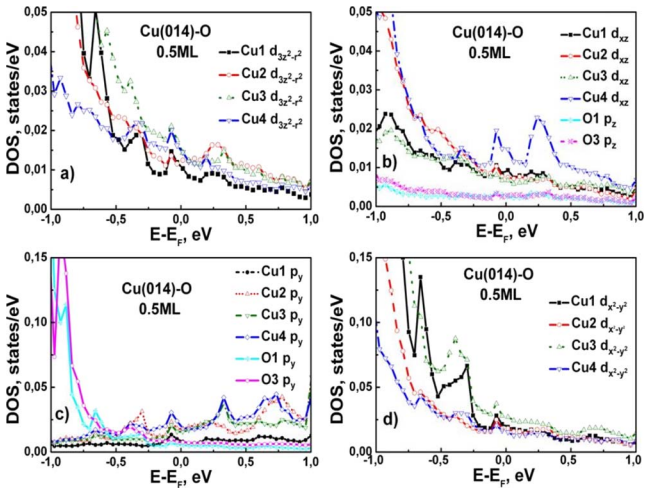

FIG. 6. (Color online) Density of electron states associated with different orbitals of copper and oxygen atoms for the Cu(014)-O surface at half-monolayer coverage: (a) Cu $d_{3z^2-r^2}$ states, (b) Cu d_{xz} and O p_z states, (c) Cu p_y and O p_y states, and (d) Cu $d_{x^2-y^2}$ states.

visualization, we have also calculated partial electron densities of states (DOS) associated with different surface atoms within the TB method.

B. Tight-binding calculations of the electronic structure of Cu(014)-O surface and MnNi tips

To calculate the electronic structure of the oxidized Cu surface, we have employed the tight-binding method where the Hamiltonian is written as

$$H = \sum_{k,\lambda} \varepsilon_{k\lambda} c_{k\lambda}^{\dagger} c_{k\lambda} + \sum_{\substack{k,l \\ \lambda,\mu}} t_{k\lambda,l\mu} c_{k\lambda}^{\dagger} c_{l\mu}, \tag{1}$$

where subscripts (k,l) label different atoms, λ and μ denote different atomic orbitals, $c_{i\lambda}^{+}$ is the creation operator of an electron occupying the orbital of type λ at the ith atom, $\varepsilon_{i\lambda}$ is the energy of the corresponding orbital, and $t_{i\lambda,j\mu}$ are the hopping coefficients.

In the TB Hamiltonian for the Cu(014)-O surface ("overlayer" model without surface atom relaxations), we took into account the first and second nearest-neighbor interactions for Cu-Cu and nearest-neighbor interaction for Cu-O. The tight-binding basis consisted of valence s, p, and d orbitals for Cu and p orbitals for O. In all calculations, Cu atoms were assumed to have the same positions as in the bulk fcc Cu (a =3.6074 Å), i.e., no surface reconstruction was taken into account. The Cu on-site energies and Cu-Cu Slater-Koster parameters were taken from Ref. 39 for the orthogonal two-center version of the tight-binding method, while the relevant parameters for Cu-O interaction were set to the values employed in Ref. 40.

The Cu(014)-O surface was modeled by a 14 Å thick slab with the primitive cell containing a total of 36 atoms (34 Cu and 2 O atoms). The electron partial DOS associated with different orbitals of Cu and O atoms is depicted in Fig. 6.

The MnNi tip electronic structure was described by the Hamiltonian

$$H_t = \sum_{k,\lambda,\sigma} \varepsilon_{k\lambda\sigma}^{(t)} c_{k\lambda\sigma}^{\dagger} c_{k\lambda\sigma} + \sum_{\substack{k,l \\ \lambda,\mu,\sigma}} t_{k\lambda,l\mu}^{(t)} c_{k\lambda\sigma}^{\dagger} c_{l\mu\sigma}, \tag{2}$$

where subscripts (k,l) label tip atoms, λ and μ denote different atomic orbitals, $c_{i\lambda\sigma}^{+}$ is the creation operator for electron with spin σ occupying the orbital of type λ at the ith atom, $\varepsilon_{i\lambda\sigma}$ is the energy of the corresponding orbital, and $t_{i\lambda,j\mu}$ are the hopping coefficients. The tight-binding basis consisted of only d orbitals of the Mn and Ni atoms. At room temperature, MnNi has a tetragonal CuAu-I-type cell which is very close to the cubic one [a=3.714 Å, c=3.524 Å (Refs. 41 and 42)]. If Mn and Ni atoms are not distinguished, this structure is very close to a fcc lattice (consisting of alternating Mn and Ni layers normal to the c axis). In bulk MnNi, Mn atoms are known to have a large magnetic moment $\mu_{\mathrm{Mn}} \sim 4\ \mu_B$ and are antiferromagnetically ordered in each layer. To describe the antiferromagnetism of the Mn sublattice in the tight-binding method, the energies of d orbitals of Mn atoms belonging to the "spin-up" sublattice (labeled by superscript I below) and "spin-down" sublattice (labeled by superscript II) were assumed to be $\varepsilon_{\mathrm{Mn}\uparrow}^{\mathrm{I}} = \varepsilon_{\uparrow}$, $\varepsilon_{\mathrm{Mn}\downarrow}^{\mathrm{I}} = \varepsilon_{\downarrow}$, $\varepsilon_{\mathrm{Mn}\uparrow}^{\mathrm{II}} = \varepsilon_{\downarrow}$, and $\varepsilon_{\mathrm{Mn}\downarrow}^{\mathrm{II}} = \varepsilon_{\uparrow}$. Thus, we have neglected the splitting of atomic d levels by the crystal field since for metal atoms in the vicinity of the tip apex, the symmetry of their local neighborhood can be substantially different from that in the bulk and therefore the atomic orbital efficient energies can strongly differ from the bulk values. Since the magnetic moment of Ni atoms is small ($\mu_{\mathrm{Ni}} < 0.6\ \mu_B$), the energy of all Ni d orbitals was taken to be equal to the same value $\varepsilon_{\mathrm{Ni}}$. The probe tip was modeled by clusters which had the shape of a tetrahedral (with the axis along [001]) and trihedral (with the edges along the diagonals of the cube distorted by shrinking along the c axis with the coefficient a/c=1.054) pyramid consisting of several hundred atoms; for the triangular pyramid, its axis was close to the [111] direction. The spatial arrangement of atoms in the pyramids was taken to be exactly the same as in the ideal bulk MnNi lattice, i.e., we have completely ignored possible relaxation of the atomic structure of the tip near its apex. Since the atomic positions in bulk MnNi are very close to the fcc lattice, in the Hamiltonian (2), we have taken into account the first 12 nearest neighbors for each atom, i.e., four atoms of the same type in the horizontal layer and eight atoms of the opposite type in vertical planes. The parameters $\eta_{dd\sigma}$=−16.2, $\eta_{dd\pi}$=8.75, and $\eta_{dd\delta}$=0, which determine for pure metals the hopping coefficients $t_{i\lambda,j\mu}$ through the matrix elements $V_{ddm} = \eta_{ddm} \frac{\hbar^2 r_d^2}{m d^{3/2}}$, $m = \sigma, \pi, \delta$, were taken from the tables of Harrison[43] and also corresponded to the case of bulk metals [the values of r_d for Mn-Mn and Ni-Ni hops were taken to be r_d^{Mn}=0.86 and r_d^{Ni} =0.71 Å, respectively, while for Mn-Ni hops, we used $r_d = r_d^{\mathrm{MnNi}} = (r_d^{\mathrm{Mn}} r_d^{\mathrm{Ni}})^{1/2}$]. With the adopted parameters of the tight-binding Hamiltonian (2), $\varepsilon_{\uparrow}$=−3 eV, $\varepsilon_{\downarrow}$=2 eV, and $\varepsilon_{\mathrm{Ni}}$=−4 eV, these gave for the bulk case the magnetic moment of Mn atoms equal to 3.45 μ_B.

The purpose of the tip calculations was to find the partial electron DOS at the probe apex atom separately for all d orbitals. In all cases, the quantization axis for both orbital and spin moments was chosen along the normal to the atomic layers forming the pyramid. To obtain the histogram for the density of states for a particular orbital, the energy axis was divided into intervals of about 40 meV in width. For a specific atomic orbital included in the TB basis, the density of states was proportional to the sum of the squared coefficients at that orbital in all eigenfunctions with energies belonging to the particular energy interval. Both tetrahedral and trihedral pyramids were analyzed in two versions, with Ni and Mn atoms at the vertex. The number of atomic layers in the pyramids did not exceed 12 (the trihedral pyramid in that case consisted of 364 atoms). The obtained results revealed that although the partial DOS for the orbitals localized at the tip apex atom is still sensitive to the cluster size, the calculated densities of states clearly show some characteristic features which are common to all sufficiently large clusters.

In the simplest approximation, the current flowing through the scanning tunneling microscope probe is governed by the density of electron states associated with the orbitals localized at the apex atom. Therefore, if one chooses the x or y axis in the surface of the studied sample along one of the typical direction (for example, along one of the close-packed rows), i.e., binds it to the sample, the observed asymmetry in atomically resolved images [W(100)-O surface] or splitting of atomic features in one of the directions [Cu(014)-O surface] can be related to possible asymmetry of the density of states at the d_{xz} and d_{yz} orbitals at the apex atom. For example, if the density of states of the d_{yz} orbital substantially exceeds that of the d_{xz} orbital, the characteristic butterflylike shape of the d_{yz} could result in the doubling of apparently seen close-packed rows of Cu(014)-O. In this case, the STM image presented in Fig. 3 can reflect the electronic structure of the MnNi tip in a similar way as tunneling spectra taken from Cu(111) surface provide information about localized electronic states of sharp fcc W tips.[44]

Let us now turn to the analysis of the DOS for different types of MnNi pyramids. The tetrahedral pyramid with a Mn atom at the apex possesses C_{4v} symmetry, and the DOS associated with the d_{xz} and d_{yz} orbitals are identical regardless of the pyramid orientation relative to the surface (i.e., regardless of the angle of rotation of the pyramid about its axis). However, the situation is completely different for the three remaining types of pyramids. For example, if we consider a tetrahedral pyramid with the Ni atom at the apex, its symmetry is reduced to C_{2v} since the second atomic layer in that pyramid consists of four Mn atoms positioned at the corners of a square and the diagonals of this square feature Mn atoms with opposite magnetic moments. Therefore, the symmetry adapted linear combinations of d_{xz} and d_{yz} orbitals belonging to different irreducible representations of C_{2v} correspond to the orbitals oriented along these diagonals. Hence, $\rho_{d_{xz}}$ will only coincide with $\rho_{d_{yz}}$ if the x and y axes are chosen parallel to the square sides in which case the symmetrized orbitals yield equal contributions to both d_{xz} and d_{yz} orbitals. The difference between $\rho_{d_{xz}}$ and $\rho_{d_{yz}}$ becomes largest when the x and y axes are chosen along the square diagonals and for that case the indicated densities of states are shown in Fig. 7(a).

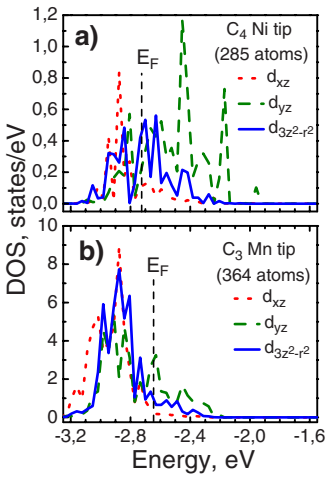

FIG. 7. (Color online) (a) Density of states for different orbitals associated with the Ni atom positioned at the tip of a tetrahedral pyramid with the axis along the [001] direction. The pyramid contains nine atomic layers and consists of 285 atoms (165 Ni atoms and 120 Mn atoms). E_F=−2.72 eV (marked by vertical dashed line). (b) Density of states for spin-up electrons at different orbitals associated with the Mn atom positioned at the tip of a trihedral pyramid. The pyramid contains 11 atomic layers and consists of 364 atoms (182 Ni atoms and 182 Mn atoms). E_F=−2.64 eV (marked by vertical dashed line).

However, the most impressive picture occurs for the trihedral pyramid with the Mn (for definiteness, spin-up) atom at the tip where the second atomic layer lying just above the apex atom is actually a triangle consisting of two Ni atoms and one Mn spin-down atom and the symmetry is reduced to C_s corresponding to reflection in the plane orthogonal to the straight line passing through the two Ni atoms. If that line is chosen as the y axis of our reference frame, the d_{xz} and d_{yz} orbitals of the apex atom belong to different representations of C_s and, consequently, should not be expected to have equal densities of states for a particular energy. Indeed, the performed calculations reveal that for the indicated reference frame orientation, in the energy range of ±50 meV around the Fermi energy (E_F), the DOS related to the d_{yz}-orbital $\rho_{d_{yz}}$ strongly exceeds both $\rho_{d_{xz}}$ and $\rho_{d_{3z^2-r^2}}$ [Fig. 7(b)]. The STM images of the Cu(014)-O surface showing the doubling of apparently seen atomic features (Fig. 3) were taken at small negative bias voltages of −30 mV corresponding to tunneling of electrons into the tip states just above the Fermi level, which is consistent with the dominance of $\rho_{d_{yz}}$ over both $\rho_{d_{xz}}$ and $\rho_{d_{3z^2-r^2}}$ around E_F.

As to the trihedral tip with the Ni atom at the apex, it also exhibits $\rho_{d_{xz}} \neq \rho_{d_{yz}}$, although this difference is not so spectacular as for the tip ending with a Mn atom.

C. Density functional theory calculations

DFT calculations were performed using the plane-wave pseudopotential code CASTEP.[45] The calculations were performed within the generalized gradient approximation using

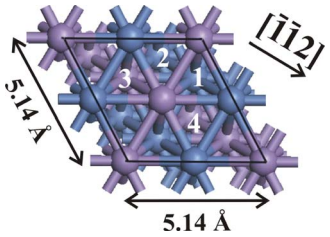

FIG. 8. (Color online) Top view of the MnNi(111) slab, showing the four threefold hollow sites on the (111) surface. The purple atoms are Mn and the blue atoms are Ni. Sites 1 and 3 are hcp sites, while sites 2 and 4 are fcc sites.

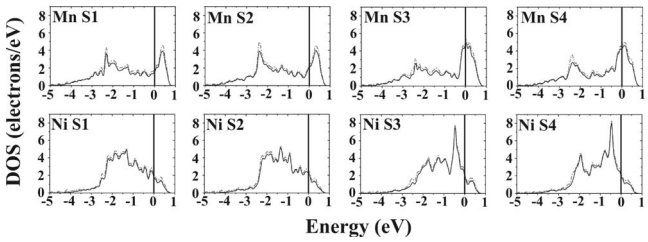

FIG. 9. Calculated local density of states (LDOS) for Mn and Ni apex atoms located at the four different coordination sites (S1, S2, S3, and S4) on the MnNi(111) surface indicated in Fig. 8. The total LDOS (dashed line) and the *d*-state contributions (solid line) are shown. Energies are displayed relative to the Fermi energy.

the gradient-corrected Perdew-Wang (GGA-PW-91) exchange-correlation functional[46] and ultrasoft Vanderbilt pseudopotentials.[47] The MnNi bulk crystal with CuAu-I-type structure (symmetry group $P4/mmm$) was simulated using the experimentally obtained lattice parameters of $a=3.74$ Å and $c=3.52$ Å.[41,42] The validity of the calculations was tested by performing spin-polarized calculations on the possible bulk magnetic structures described by Sakuma.[48] The antiferromagnetic (AF)-I-type structure was found to be the ground state magnetic structure at 171 and 56 meV/atom below the ferromagnetic and AF-II-type antiferromagnetic structures. A magnetic moment of 4.06 μ_B was obtained for the Mn magnetic moment in the AF-I structure, which compares with a theoretical value of 3.29 μ_B obtained by Sakuma[48] and experimental values of 3.8–4.0 μ_B obtained by neutron diffraction.[41,42] As the MnNi tips used in the experiments were polycrystalline, we have investigated both [111]- and [001]-oriented tips. The tip simulations were carried out without spin polarization as the magnetic order of the tip was not deemed important in the context of the experimental results.

1. MnNi(111) tip

A five-layer [111]-oriented MnNi slab was constructed, and the interlayer separation was optimized by constraining the atoms along one face of the slab and allowing the remaining layers to relax. The geometry optimization was carried out using the Broyden-Fletcher-Goldfarb-Shanno method[49] with a force convergence threshold of 0.1 eV/Å. A vacuum gap of 8 Å, plane-wave cutoff energy of 400 eV, and $3\times3\times1$ *k*-point grid were used. The optimized slab showed an outward expansion of the surface layer by 0.9% and a contraction of the second layer by 0.9% compared to the bulk interlayer spacing (2.11 Å). It was also found that the positions of the atoms in the surface layer were buckled, with Mn atoms occupying a *z* position 0.07 Å higher than the Ni atoms. Tips were simulated by placing Mn or Ni adatoms at one of the four threefold hollow sites on the surface labeled S1–S4, which are identified in Fig. 8. The apex atom was placed at an initial height of 2.1 Å above each of these sites and its position was then optimized. For these calculations, a vacuum gap of 12 Å was selected to ensure that there was no interaction between the tip atom and the rear side of the MnNi(111) slab, and the lateral dimensions of the surface cell were sufficiently large to ensure a minimum of two atom spacings between the tip atoms in adjacent cells. It was found that the Mn tip atoms lie about 0.2 Å closer to the MnNi(111) surface ($d=1.56\pm0.04$ Å) than their Ni counterparts ($d=1.75\pm0.02$ Å).

The local density of states (LDOS) of the tip as a function of coordination site and apex atom type were calculated using a plane-wave cutoff energy of 270 eV and a $4\times4\times1$ *k*-point grid. Figure 9 shows the total LDOS (dashed line) and the *d*-state contribution (solid line) around E_F for Mn and Ni apex atoms at the four different coordination sites shown in Fig. 8. Clearly, the LDOS of the apex atom is largely insensitive to whether it occupies a fcc or hcp coordination site but rather depends on the chemical nature of its nearest neighbors. The highest LDOS values at E_F are obtained for Mn atoms occupying sites S3 and S4 (i.e., a threefold hollow site comprising one Mn atom and two Ni atoms), as the LDOS peak for these tip atoms is centered at E_F. For Mn apex atoms located at sites S1 and S2 (i.e., a threefold hollow comprising one Ni atom and two Mn atoms), the LDOS peak is situated 0.3–0.4 eV above E_F. The LDOS values measured at E_F for these tips are lower and are similar to those obtained for Ni apex atoms. Large LDOS peaks are obtained at 0.5 eV below E_F for Ni apex atoms located at the S3 and S4 sites, while a broad distribution of states is obtained for Ni atoms located at the S1 and S2 sites. The variation in LDOS of the same apex atom at different coordination sites has particular implications for the stability of the tip when obtaining atomically resolved images. For example, for STM measurements performed in the energy interval $E_F\pm0.2$ eV, the most substantial change in tunneling probability and therefore tunnel current would be observed if a Mn apex atom hopped between coordination sites S3 to S1 on the tip surface. Obviously, such diffusion of the apex atom across the surface of the tip can quite feasibly occur while the tip scans a sample surface, in much the same way that tip-induced diffusion of atoms on sample surfaces occurs.[50]

We are also interested in the shape of the tip orbitals protruding into vacuum. Figure 10 shows orbital maps for Mn and Ni apex atoms in the energy interval $E_F\pm0.22$ eV. The maps are displayed in a vertical slice through the vacuum slab along the [$\bar{1}\bar{1}$2] direction and horizontal (111) slices through the apex atom and 0.5 Å above it. The *z* direction, corresponding to the crystallographic *c* axis or the [001] direction, as well as the *x* and *y* directions are oriented

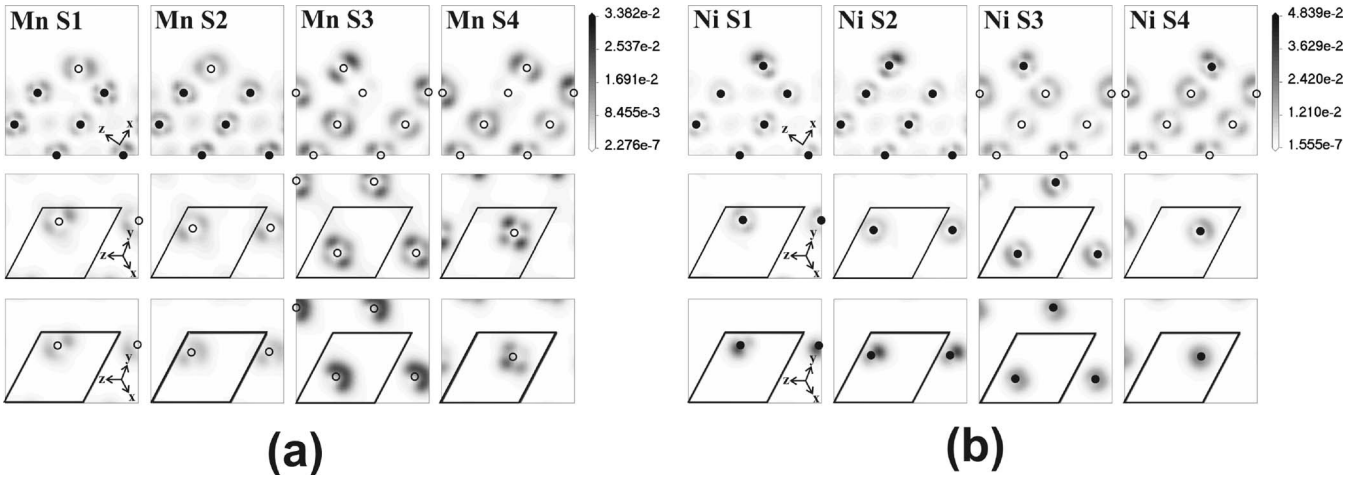

FIG. 10. Orbital maps displaying the electron density (electrons/Å^3) in the energy interval $E_F \pm 0.22$ eV for (a) Mn and (b) Ni apex atoms at four different coordination sites (S1, S2, S3, and S4) on the MnNi(111) surface. The maps in the upper panels are displayed in a vertical cut through the vacuum slab along the $[\bar{1}\bar{1}2]$ direction. The middle panels show a horizontal (111) slice through the apex atom. The unit cell of the slab surface is indicated. The lower panels show a horizontal slice 0.5 Å above the apex atoms. The positions of Mn atoms are indicated by empty circles and Ni atoms by solid circles. The x, y, and z axes are oriented along the $\langle 001 \rangle$ directions of the MnNi bulk.

out of the surface plane. Taken together, the three-dimensional shape of the tip orbital can be inferred. For example, the MnS3 tip displays d_{xy} character with four lobes lying in the x-y plane, while the MnS4 tip displays d_{xz} or d_{yz} character. Overall, Mn or Ni tips in the S3 or S4 coordination sites appear to yield the sharpest contours with a single lobe of electron density protruding into vacuum and would therefore be expected to produce the highest resolution as STM tips. On the other hand, the MnS1 tip produces twin lobes protruding into vacuum above the apex atom. The asymmetric character of this tip compared with the others is best illustrated by the charge density isosurfaces plotted for each of the Mn-terminated tips shown in Fig. 11. This asymmetric character would be particularly suited to producing the atomic doubling and asymmetric imaging observed experimentally on the Cu(014)-O and W(100)-O surfaces, respectively.

2. MnNi(111) tip/Cu(111)-O surface

To investigate the interaction of these tips with an oxygen-covered surface, an STM junction was simulated using a three-dimensional supercell comprising an oxygen-covered pseudomorphic five-layer Cu(111) slab attached to the reverse side of the MnNi tip slab. Oxygen adatoms were optimized at 1.15 Å above fcc hollow sites in a (2×2) configuration on the Cu(111) surface. The apex atom of the tip was positioned directly over an oxygen adatom, and the vacuum gap between them was varied between 2 and 9 Å. While the simulation is limited to a fixed tip position relative to the surface, i.e., the surface is not scanned by the tip, it provides useful information on the tip characteristics close to the surface. Figure 12 shows the calculated tip DOS as a function of the vacuum gap for Mn- and Ni-terminated tips. The calculations were performed with a cutoff energy of 340 eV and a $6\times6\times1$ k-point grid. It is important to note that these calculations do not take into account the relaxation of the tip when it is in close proximity to the surface, or vice versa. However, as will be shown later, we have performed calculations for junctions where the mechanical tip-surface interaction has been taken into account, which give qualitatively similar results. The results are displayed for vacuum gaps of 2, 3, or 4 Å, i.e., where the tip effectively comes into contact with the surface. By reducing the vacuum gap from 3 to 2 Å, the O $2p$ peak shifts by 0.5–0.6 eV to lower energies, which is generally accompanied by a reduction in the metal $3d$ states near the Fermi energy. For larger vacuum

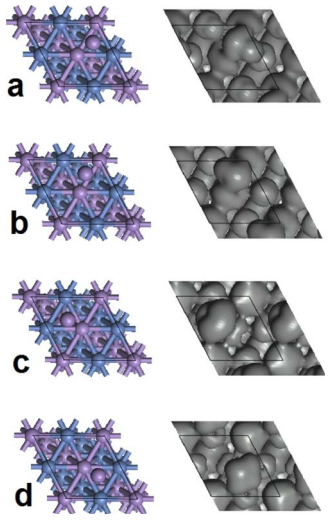

FIG. 11. (Color online) Schematic models and calculated electron density isosurfaces for (a) MnS1, (b) MnS2, (c) MnS3, and (d) MnS4 tip configurations. The model of the tip is presented on the left and shows the relative position of the tip atom on the surface. The corresponding isosurface is shown on the right and displays the calculated electron density at 2.4×10^{-3} electrons/Å^3 in the $E_F \pm 0.22$ eV energy range.

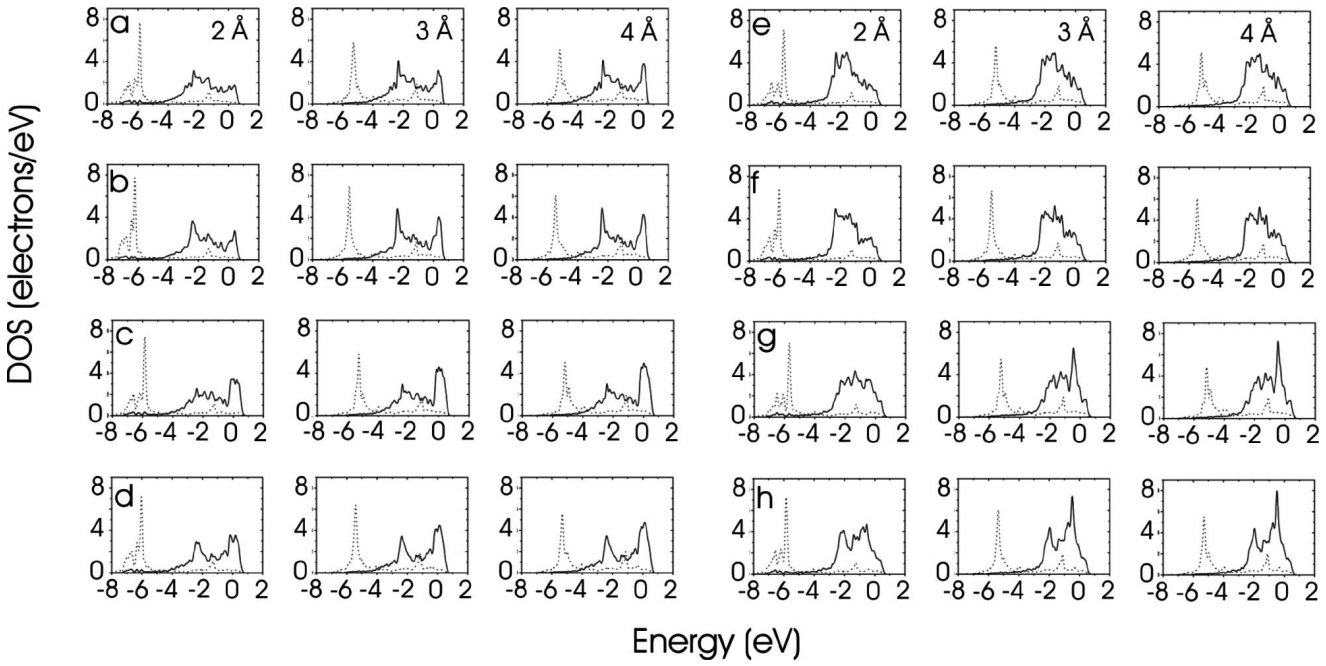

FIG. 12. Combined apex atom *s*, *p*, and *d* states near E_F (solid line) and oxygen adatom 2*p* states (dotted line) for vacuum gaps of 2, 3, and 4 Å. (a) MnS1, (b) MnS2, (c) MnS3, (d) MnS4, (e) NiS1, (f) NiS2, (g) NiS3, and (h) NiS4.

gaps (i.e., 6–9 Å), the Cu(111)-O surface was not found to perturb the electronic structure of the tip significantly.

We have performed charge density difference calculations to visualize the redistribution of the electron density around the apex atom and oxygen adatom as the tip comes into contact with the surface. A representative example is shown in Fig. 13 for a Mn apex atom located at site S1 with vacuum gaps of 4 and 2 Å. The valence electrons surrounding the oxygen adatom shift away from the atom core. Some move closer to the Cu(111) surface, resulting in enhanced back bonding to the Cu(111) surface, which is responsible for the 2*p* peak shift in the LDOS. Others spill out into the vacuum gap between the adatom and the tip, resulting in an enhanced corrugation of the surface LDOS. The latter effect is negated to some extent by the redistribution of charge around the apex atom of the tip. There is a net reduction in charge spilling into the vacuum gap as some of the charge shifts into the (111) plane around the atom, while the remainder goes to enhancing the back bonding to the MnNi(111) surface. This trend is typical of all the tips studied as reflected in the corresponding orbital maps of each tip-surface interface. Figure 14 shows for each tip the calculated electron density associated with the set of orbitals in the energy range $E_F \pm 0.22$ eV for a tip-surface gap of 2 Å. For apex atoms located at coordination sites S1 and S2, the electron density protruding from the tip into the vacuum gap is reduced, giving rise to a node in electron density directly above the atom core and producing twin lobes protruding into vacuum on either side of it. The effect is less pronounced for apex atoms located at sites S3 and S4 but is still present, e.g., the prominent lobe above NiS4 in Fig. 10 is reduced and moves closer to the (111) plane in Fig. 14.

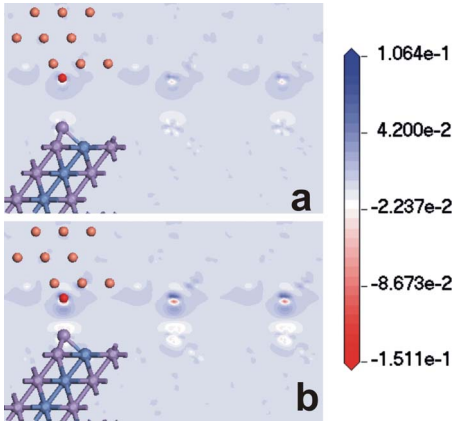

FIG. 13. (Color online) Charge density difference contour maps (displayed in electrons/Å^3) at the tip-surface interface for (a) a 4 Å vacuum gap and (b) a 2 Å gap. The tip configuration used is a Mn apex atom located at coordination site S1 on the MnNi(111) surface. Blue spheres denote Ni atoms, purple spheres denote Mn atoms, copper spheres denote Cu atoms, and the red sphere denotes the oxygen adatom.

To investigate the effect of the mechanical tip-surface interaction, we have performed geometry optimization for the STM junctions comprising the MnS1 and NiS1 tips. For this, we have used similar optimization parameters to those described above for the preoptimized tips. The positions of the tip apex atom, oxygen atom, and uppermost two layers of the MnNi(111) and Cu(111) surfaces were allowed to relax. The results for initial vacuum gaps of 2, 4, and 8 Å are presented in Table I and show that the vacuum gap in all cases decreases due to the attractive tip-surface interaction.

The calculated charge density maps in the energy range $E_F \pm 0.22$ eV for the fully relaxed systems with initial tip-

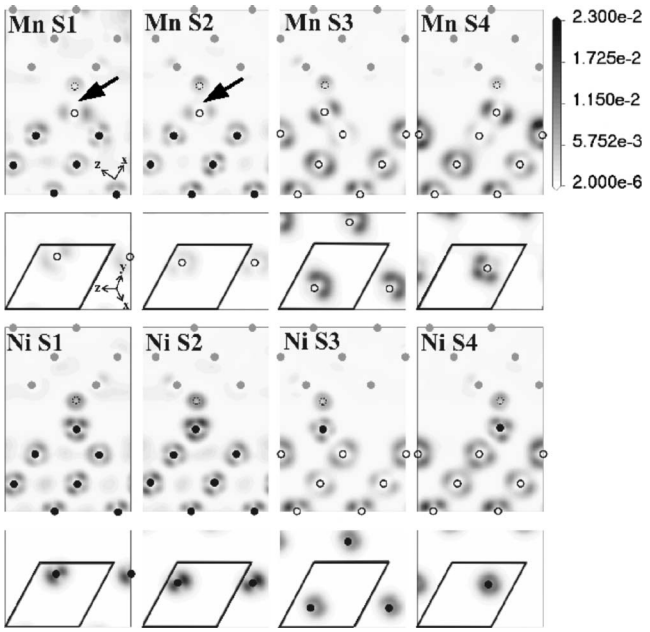

FIG. 14. Orbital maps displaying the electron density (electrons/Å^3) in the energy interval $E_F \pm 0.22$ eV for Mn and Ni terminated MnNi(111) tips positioned 2 Å above an oxygen adatom on the $c(2\times2)$ Cu(111)-O surface. The maps in the upper panels are displayed in a vertical cut through the vacuum slab along the $[\bar{1}\bar{1}2]$ direction. The arrows in the panels for MnS1 and MnS2 indicate the position of the node in electron density above these two tips. The lower panels show a horizontal cut, i.e., (111) slice, located 0.5 Å above the position of the apex atom. The unit cell of the surface is indicated. The positions of Mn atoms are indicated by empty circles, the Ni atoms by solid circles, the Cu atoms by gray circles, and the oxygen adatom by a dashed circle.

surface gaps of 2, 4, and 8 Å are shown in Fig. 15. Comparing these results with those shown in Fig. 14 (and also Fig. 10 for the case of no tip-surface interaction), it is clear that they are qualitatively similar to those obtained for the less computationally expensive preoptimized tip-surface combinations. We therefore believe that the latter are a reasonably

TABLE I. Calculated interlayer distances (given in Å) for the fully relaxed tip-surface systems for MnS1 and NiS1 tips over the Cu(111)-O surface with an initial gap ($\Delta_{initial}$) of 2, 4, or 8 Å. Δ_{gap} is the value of the relaxed tip-surface separation, Δ_{apex} is the distance of the apex atom from the MnNi(111) surface, and Δ_{oxygen} is the distance of the oxygen adatom above the Cu(111) surface. $\Delta_{MnNi(1)}$, $\Delta_{MnNi(2)}$, $\Delta_{Cu(1)}$, and $\Delta_{Cu(2)}$ are the first two interlayer separations of the MnNi(111) and Cu(111) surfaces, respectively.

Apex atom	$\Delta_{initial}$	Δ_{gap}	Δ_{apex}	$\Delta_{MnNi(1)}$	$\Delta_{MnNi(2)}$	Δ_{oxygen}	$\Delta_{Cu(1)}$	$\Delta_{Cu(2)}$
Mn	2	1.81	1.78	2.08	2.09	1.27	1.98	2.02
Mn	4	2.32	2.37	2.22	2.27	1.66	2.00	2.20
Mn	8	7.60	1.94	2.14	2.14	1.16	2.15	2.05
Ni	2	1.81	1.82	2.10	2.13	1.31	2.00	2.07
Ni	4	3.76	1.81	2.13	2.16	1.25	2.02	2.10
Ni	8	7.83	1.79	2.13	2.15	1.24	2.01	2.11

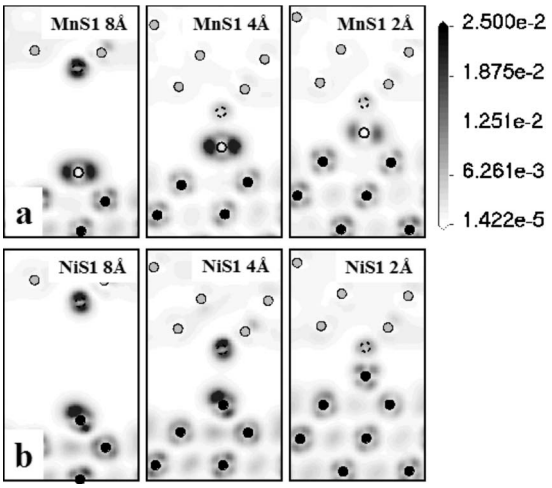

FIG. 15. Orbital maps displaying the electron density (electrons/Å^3) in the energy interval $E_F \pm 0.22$ eV for the fully relaxed system of (a) MnS1 and (b) NiS1 tips initially positioned 8, 4, and 2 Å above an oxygen adatom on the $c(2\times2)$ Cu(111)-O surface. The maps are displayed in a vertical cut through the vacuum slab along the $[\bar{1}\bar{1}2]$ direction.

good representation of the tip behavior in the fully relaxed systems in all cases for both (111) and (001) tips.

3. MnNi(001) tip

Five-layer slabs were constructed for both the Mn- and Ni-terminated MnNi(001) surfaces. The interlayer separations were optimized in the manner described for the MnNi(111) tip slab, using a plane-wave cutoff energy of 400 eV and a $4\times4\times1$ k-point grid. The Mn-terminated surface showed a contraction of the surface layer by 1.1% and an expansion of the second layer by 0.6% compared to the bulk interlayer spacing (1.76 Å), while the Ni-terminated surface displayed a substantial contraction of the first layer by 13.6%, while the second layer was also contracted by 1.1%. Tips were simulated by placing either Mn or Ni apex atoms 1.3 Å above fourfold hollow sites on either surface and optimizing the position of the atom. A (2×2) surface cell was adopted for this purpose to minimize lateral interactions between the apex atoms in adjacent cells. The Ni apex atoms relaxed to 1.49 ± 0.01 Å above either surface, while the Mn apex atoms relaxed to a height of 1.27 ± 0.01 Å.

The LDOS around E_F was calculated for each tip, and the results are shown in Fig. 16. As only one type of fourfold coordination site is present on the (001) surface, it is clear that a [001]-oriented MnNi tip is preferable to a [111]-oriented tip, since the LDOS of the apex atom will not change if it moves between adjacent sites. In the energy interval $E_F \pm 0.22$ eV, apex atoms on the Ni-terminated surface possess a higher LDOS than their counterparts on the Mn-terminated surface and can therefore be expected to produce larger tunnel currents. The shape of the tip orbitals in the energy interval $E_F \pm 0.22$ eV is shown in Fig. 17. The orbital maps in the upper panel are displayed as slices taken along the [100] direction of the vacuum slab, while the lower panel

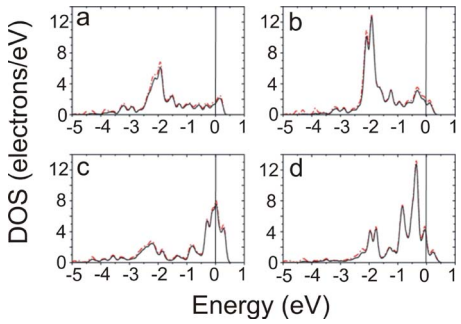

FIG. 16. (Color online) Calculated local density of states (LDOS) for Mn and Ni apex atoms located at fourfold hollow sites on the Mn- and Ni-terminated MnNi(001) surfaces. The total LDOS (dashed line) and the *d*-state contributions (solid line) are shown. Energies are displayed with respect to the Fermi energy. (a) Mn atom on Mn-terminated (001) surface, (b) Ni atom on Mn termination, (c) Mn atom on Ni termination, and (d) Ni atom on Ni termination.

maps display (001) slices taken through the apex atom and 0.5 Å above it. The Mn on Ni-terminated MnNi(001) tip displays $d_{x^2-y^2}$ character in the (001) plane, while the other tips display d_{xy} character. With the exception of the Ni on Ni-terminated MnNi(001) tip, the tips display single lobes protruding into vacuum. The latter displays a node in electron density above the apex atom. The Mn on Mn-terminated MnNi(001) tip shows the highest electron density and sharpest contour protruding into vacuum and would therefore be expected to provide the highest resolution.

4. MnNi(001) tip/Cu(001)-O surface

The interaction of the MnNi(001) tip with a $c(2\times2)$ Cu(001)-O surface was investigated in the same manner as that described for the MnNi(111) case. A five-layer Cu(001) slab with a $c(2\times2)$-O chemisorbed layer was attached pseudomorphically to the rear side of the MnNi(001) slab, so that the apex atom of the tip was positioned directly over the oxygen adatom in the adjacent cell along the *c* axis. The oxygen adatoms were optimized at 0.8 Å above the fourfold hollow sites on the Cu(001) surface. Again, the effect of the proximity of the oxygen atom on the electronic structure of the tip apex was investigated by varying the vacuum gap between the apex atom and the oxygen adatom between 2, 3, and 4 Å. The calculations were performed with a cutoff energy of 300 eV and a $3\times3\times1$ *k*-point grid, and again we do not consider the relaxation of the tip in close proximity to the surface. The calculated LDOS of the apex atom and oxygen adatom near E_F as a function of the vacuum gap are presented in Fig. 18, while the orbital maps in the energy range $E_F\pm0.22$ eV are shown in Fig. 19. The general behavior is the same as was observed for the [111]-oriented tips, with a redistribution of the charge around the tip into the MnNi(001) surface, i.e., away from the vacuum gap, as the tip comes within 2 Å of the Cu(001)-O surface. This results, for example, in the formation of a node in the electron density over a Mn apex atom on Ni-terminated MnNi(001), cf. Fig. 19(b). However, the interaction with the surface does not produce an asymmetric tip state capable of producing the experimentally observed atomic doubling on Cu(014)-O and

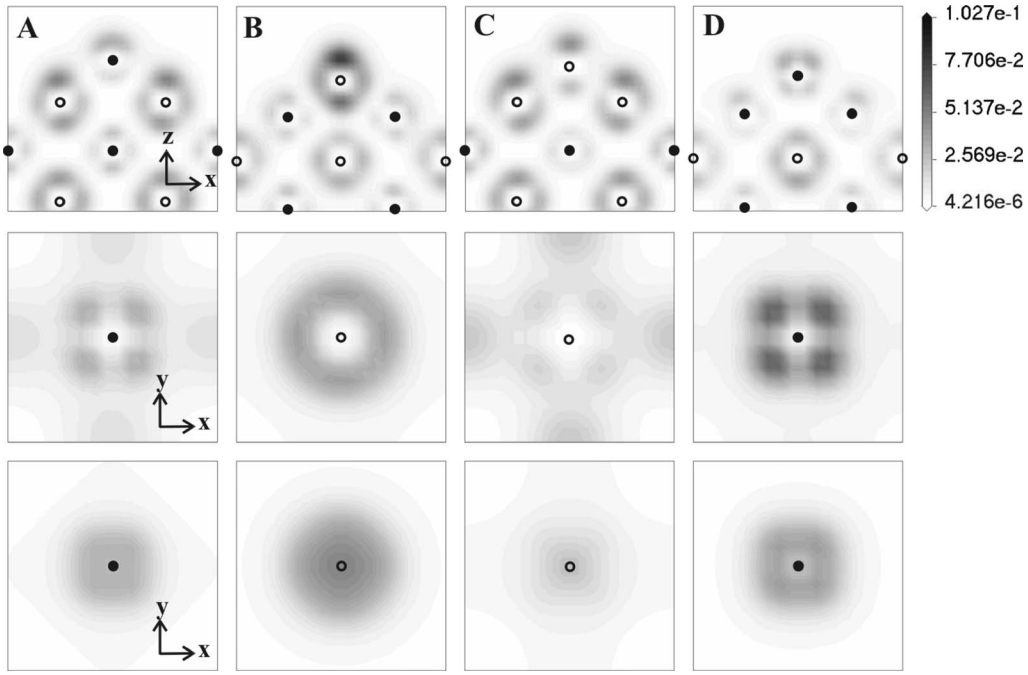

FIG. 17. Orbital maps displaying the electron density (electrons/Å^3) in the energy interval $E_F\pm0.22$ eV for [001]-oriented MnNi tips. (a) Ni apex atom on Mn termination, (b) Mn atom on Ni termination, (c) Mn atom on Mn termination, and (d) Ni atom on Ni termination. The upper panels are displayed in a vertical cut through the vacuum slab along the [100] direction. The middle panels are shown in a horizontal (001) slice that bisects the apex atom. Note that the color scale only applies to the upper panels. The lower panels are shown in a horizontal (001) slice located 0.5 Å above the positions of the apex atoms. The positions of Mn atoms are indicated by empty circles and Ni atoms by solid circles.

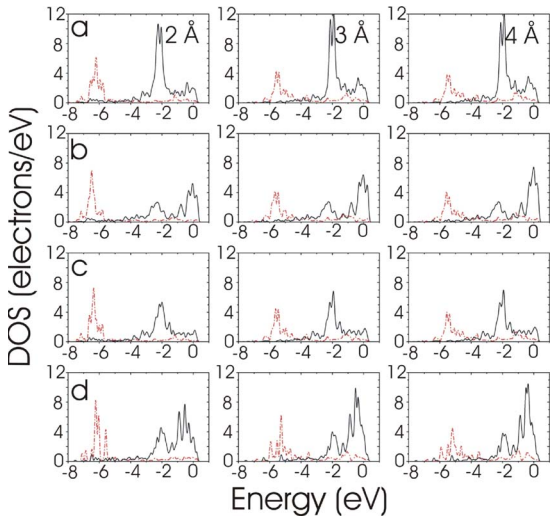

FIG. 18. (Color online) Calculated local density of states (LDOS) for [001]-oriented MnNi tips positioned 2, 3, and 4 Å above a Cu(001) (2×2)-O surface, respectively. The apex atom combined s, p, and d states near E_F (solid line), and oxygen adatom $2p$ states (dotted line) are shown for (a) Ni apex atom on Mn-terminated (001) surface, (b) Mn apex atom on Ni termination, (c) Mn apex atom on Mn termination, and (d) Ni atom on Ni termination. Energies are displayed relative to the Fermi energy.

asymmetric imaging on W(100)-O. We therefore conclude that a [111]-oriented tip was responsible for these images.

D. Tip-surface distance dependence of the Cu(014)-O scanning tunneling microscopy images

The results of the theoretical consideration of the coupled tip-surface systems[21] demonstrated a possibility of d_{xz}, d_{yz}, d_{xy}, and $d_{x^2-y^2}$ orbital contributions at small tip-surface separations (low gap resistances). Moreover, the results of the local electron density of states calculations[21] revealed that the contribution of electron states with axial (d_{xz},d_{yz}), and nodal (d_{xy}, and $d_{x^2-y^2}$) symmetries could give enhanced (compared with $d_{3z^2-r^2}$ orbitals) atomic corrugations in STM images. It should be mentioned, however, that the theoretical results[21] predicted that the effect of corrugation enhancement can be drastically reduced in the case when the relative contribution of electron states with $m=0$ (s or $d_{3z^2-r^2}$ orbitals) becomes significant. In this case, asymmetry in the atomic features can be observed[23,25] in the surface regions where the electron density associated with $m\neq0$ states substantially exceeds that for states with $m=0$. This situation is likely to occur for the Cu(014)-O surface containing four nonequivalent copper atomic rows and atoms of different chemical nature. As an example, Fig. 20 displays a comparison of partial electron DOS associated with different d orbitals of the same surface atoms. This figure demonstrates domination of $d_{x^2-y^2}$ states on copper atoms in the first and third terrace rows in the vicinity of E_F, while the partial DOS values for different orbitals of the second and fourth row atoms are rather similar. Results of TB calculations presented in Fig. 20 suggest a nonuniform spatial distribution of the electron DOS associated with different d states for the studied Cu(014)-O system.

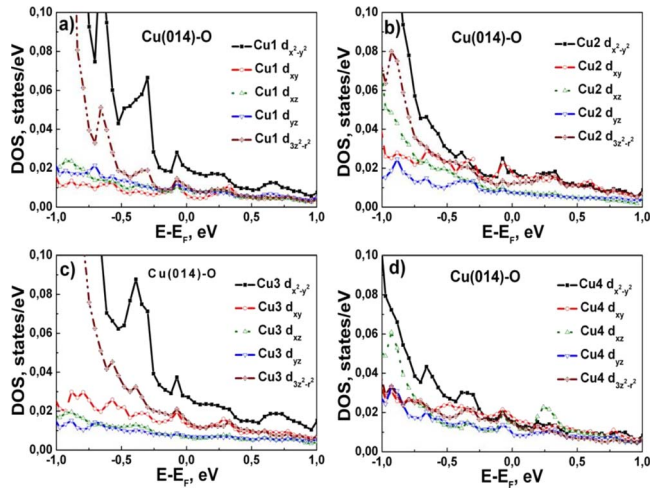

FIG. 20. (Color online) Partial electron DOS associated with copper atoms in the (a) first, (b) second, (c) third, and (d) fourth terrace rows of the Cu(014)-O surface.

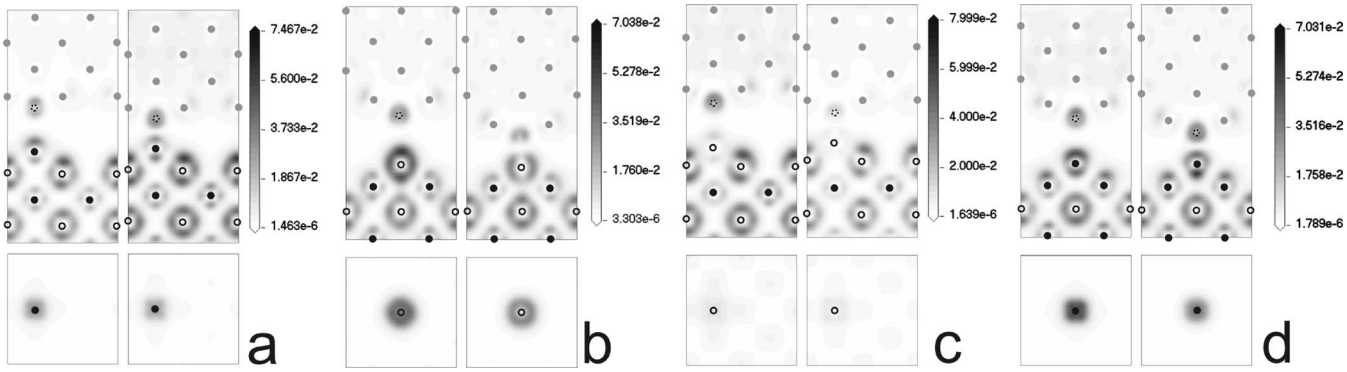

FIG. 19. Orbital maps displaying the electron density (electrons/Å^3) in the energy interval $E_F\pm0.22$ eV for [001]-oriented MnNi tips positioned 3 and 2 Å over a Cu(001) (2×2)-O surface, respectively. (a) Ni apex atom on Mn termination, (b) Mn atom on Ni termination, (c) Mn atom on Mn termination, and (d) Ni atom on Ni termination. In each case, the upper panels are displayed in a vertical cut through the vacuum slab along the [100] direction, while the lower panels are shown in a horizontal (001) slice located 0.5 Å above the position of the apex atom. The positions of Mn atoms are indicated by empty circles and Ni atoms by solid circles.

From the experimental tip-sample distance dependence of the Cu(014)-O images (Fig. 2), one can see smaller atomic corrugations for the images measured at larger gap resistances and corrugation enhancement in the images taken at smaller gap resistances. The latter is especially pronounced in STM images presented in Figs. 2(h) and 2(j). The corrugation height enhancement for the Cu(014)-O images demonstrating one or two atomic rows within terraces in comparison with images showing three or four copper atomic rows was observed earlier in our experiments with paramagnetic W probes.[1] The results of TB calculations of the electron DOS associated with different copper and oxygen atoms of the Cu(014)-O surface demonstrate a comparable electron DOS associated with $d_{3z^2-r^2}$ orbitals of different copper atoms [Figs. 6(a)]. This result favors the suggestion that STM images of Cu(014)-O with greater number of atomic features within terraces and smaller corrugation heights could be mainly determined by the contribution of $d_{3z^2-r^2}$ orbitals associated with copper surface atoms. The partial contribution of $d_{3z^2-r^2}$ states to the STM image formation should be more significant at the largest separations. Domination of the down-step row in some images can be explained by the prevailing contribution of d_{xz} and d_{yz} orbitals at smaller tip-surface distances. As an example, Fig. 6(b) indeed demonstrates a larger calculated DOS for the d_{xz} orbitals associated with the fourth copper row atoms. The protrusions in oxygen rows (1,3) in the images of Cu(014)-O can be expected if the contribution of $d_{x^2-y^2}$ orbitals associated with copper atoms in the first and third atomic rows or $p_{x,y}$ orbitals associated with oxygen atoms becomes dominant at the smallest tip-surface separations. The largest contribution of the oxygen $p_{x,y}$ orbitals in the vicinity of the Fermi level is not so straightforward from the TB calculation results [Fig. 6(c)] and may be inferred only if the surface electronic structure is modified significantly by tip-surface interaction. At the same time, the electron DOS near the Fermi level associated with $d_{x^2-y^2}$ orbitals of copper atoms in the first and third terrace rows actually exceeds that of copper atoms in the second and fourth terrace rows [Fig. 6(d)]. The experimental data presented in Fig. 2 reveal that the relative contribution of different electron states may change significantly with a rather small reduction of the tip-sample distance. At small tunneling gaps and low bias voltages, the relation between the tunneling current and the tip-sample separation can be simplified to[51]

$$I \propto (V/d)\exp(-A\varphi^{1/2}d), \tag{3}$$

where $A=1.025$ $(\mathrm{eV})^{-1/2}$ $\mathrm{Å}^{-1}$, V is the bias voltage, φ is the barrier height (work function which is typically about 4 eV for transition metals), and d is the tip-sample distance. According to Eq. (3), the tunneling current increase from 0.08 to 0.18 nA [Figs. 2(f)–2(k)] at fixed bias voltage should correspond to a tip-surface separation reduction of approximately 0.5 Å. At the small separations required to obtain atomically resolved images of the Cu(014)-O surface, this decrease in the tip-surface distance can be sufficient to change the symmetry of electron states involved in the tunneling process. Note that theoretical simulations of Al(100) STM images obtained both with sharp and blunt Al tips[22] showed several different types of images in a rather narrow separation range from 2.34 to 3.64 Å. This was ascribed to the appearance of new tunneling channels and enhanced tunneling via p_{xy} orbitals at smaller distances. We should also mention that effects of corrugation enhancement with decreasing gap resistance can be caused by the tip-surface interaction which is substantial at small separations as illustrated by the results of DFT calculations (Table I). In particular, a relaxation of the apex atom can induce an enhancement of corrugation heights in the same way as reported for some metal surfaces (e.g., see Refs. 10–14 and references therein). In our case, the elastic forces exerted to the tip can also modify corrugation heights with decreasing tip-surface distance [(Figs. 2(g)–2(j))] though they can hardly explain the observed changes in the number of atomically resolved features within terraces. We believe that the change in the relative contribution of different electron states is most likely responsible for the symmetry change in the Cu(014)-O STM images (Fig. 2).

The presented STM data and results of numerical calculations demonstrate that different electron states of both the tip and the surface atoms should be taken into account for detailed interpretation of the experimentally measured STM images of oxygen-induced reconstructed metal surfaces. The tip-surface distance dependence of the Cu(014)-O images taken with MnNi probes and calculated electron DOS associated with surface and tip apex atoms reveal that selective imaging and splitting of atomic features in atomically resolved images of Cu(014)-O as well as asymmetry effects in the images of W(100)-O can be caused by the prevailing contribution of different electron orbitals (namely, $d_{3z^2-r^2}$, d_{xz}, d_{yz}, d_{xy}, and $d_{x^2-y^2}$) at different tunneling conditions.

The distance dependence of Cu(014)-O STM images (Fig. 2) as well as the results of TB and DFT calculations presented in previous sections allow us to suggest why clearly seen doubling of the atomic features could only be resolved in rare experiments and at certain bias voltages and tunneling currents. Due to selective imaging of the surface atoms on Cu(014)-O (dependent on the tip structure and tip-surface distance) in a real experiment, one should adjust the separation in such a way that the $d_{3z^2-r^2}$ surface states give the largest contribution to the tunneling current and apply the appropriate bias voltage where the d_{yz} orbitals dominate in the tip electronic structure. This situation is schematically shown in [Fig. 1(b)]. The separation could not be too large (the tip d_{yz} state contribution can become insufficient) nor too small (surface states with nodal symmetry can play a significant role smearing the atomic features). We suggest that the necessary separations may lie in a narrow range and that the required combination of bias voltage and tip-surface distance cannot be easily achieved in the experiment for each tip geometry. Moreover, the results of DFT and TB calculations suggest that only some tip geometries can lead to well pronounced asymmetry effects in atomically resolved images. We believe that it is the [111]-oriented MnNi tip with Mn atom located exactly at the tip apex that is responsible for observed asymmetric atomic features.

The results of DFT calculations for the interacting MnNi-tip–oxide-surface system presented in previous sections suggest that the STM images obtained with the [111]-oriented

MnNi tip can also be affected by the tip-surface interaction. This interaction at rather small tip-surface separations, in particular, can induce redistribution of the electron DOS at the tip apex resulting in asymmetry of the atomically resolved images. We suggest that the orbital orientation in our STM experiments on Cu(014)-O could be determined by a rather strong O-Mn crystal field adjusting the active orbital to one of distinguished directions in the surface plane and this is the reason why the doubling was observed only in the {110} direction.

IV. CONCLUSIONS

We have presented STM data on Cu(014)-O and W(100)-O surfaces obtained with MnNi probes and results of DOS calculations for MnNi tips with different atomic arrangements at the apex. The results of DOS calculations provide a qualitative explanation for the observed doubling of atomic features and asymmetry effects in STM images of Cu(014)-O and W(100)-O surfaces, respectively. The reported experimental and calculated data prove that the structure of the outer shell orbitals and their partial DOS at the tip apex atom play a dominant role in the nature of atomically resolved STM image formation. For the (111)-oriented MnNi tip, hopping of the apex atom between different threefold sites on the MnNi(111) surface can result in substantial changes of the tip LDOS. In contrast, a (001)-oriented tip offers much better stability in terms of obtaining atomically resolved STM images. We identify one configuration for [111]-oriented MnNi tips, namely, a Mn apex atom located at an hcp coordination site, which displays twin lobes of electron density protruding into vacuum. Such an asymmetric tip state may be responsible for the experimentally observed atomic row doubling on Cu(014)-O or asymmetric imaging of orthogonal $p(3\times1)$ missing-row domains on W(100)-O. Further asymmetric tip states are produced when [111]-oriented tips are brought to within 2 Å of an oxygen-covered Cu surface. This represents the contact regime where the vacuum gap is of the order of a bond length. In this regime, the electron density surrounding the apex atom of the tip is forced away from the vacuum gap and into the MnNi(111) surface, resulting in some cases in the formation of lobes with a nodal point directly over the position of the apex atom. A similar set of calculations performed for [001]-oriented MnNi tips indicated that no asymmetric tip states are formed. We therefore conclude that a [111]-oriented MnNi tip could be responsible for the experimentally observed effects. The tip-sample distance dependence of the Cu(014)-O STM images and results of DFT and TB calculations of the tip and surface electronic structure demonstrate that atomically resolved images in some cases can be affected by relative contribution of different electron orbitals associated both with the tip and the surface atoms. Further calculations involving simulation of STM images using the tip and sample states described above will be required in order to exactly identify the conditions that give rise to the experimentally observed images of the Cu(014)-O and W(100)-O surfaces.

ACKNOWLEDGMENTS

This work was supported by the Russian Academy of Sciences, NT-MDT (Zelenograd), Project No. MK-2370.2005.2, RSSF, and FASI grants. We thank V. N. Matveev and N. A. Vinogradova for assistance in the copper sample preparation. The support of Science Foundation Ireland (00/PI.1/C042) and the European project ASPRINT NMP-CT-2003-001601 is gratefully acknowledged. This work made use of computing facilities at the Trinity Centre for High Performance Computing, supported by IITAC, the HEA, and the National Development Plan.

[1] A. N. Chaika and S. I. Bozhko, JETP Lett. **82**, 416 (2005) [Pis'ma Zh. Eksp. Teor. Fiz. **82**, 467 (2005)]; A. N. Chaika, S. S. Nazin, and S. I. Bozhko (unpublished).
[2] S. Murphy, J. Osing, and I. V. Shvets, Appl. Surf. Sci. **144-145**, 497 (1999).
[3] S. F. Ceballos, G. Mariotto, S. Murphy, and I. V. Shvets, Surf. Sci. **523**, 131 (2003).
[4] R. Wiesendanger, H.-J. Guntherodt, G. Guntherodt, R. J. Gambino, and R. Ruf, Phys. Rev. Lett. **65**, 247 (1990).
[5] R. Wiesendanger and M. Bode, Solid State Commun. **119**, 341 (2001).
[6] S. Yu. Bulavenko, P. V. Melnik, and M. G. Nakhodkin, Surf. Sci. **469**, 127 (2000).
[7] P. Sutter, P. Zahl, E. Sutter, and J. E. Bernard, Phys. Rev. Lett. **90**, 166101 (2003).
[8] J. Tersoff and D. R. Hamann, Phys. Rev. Lett. **50**, 1998 (1983).
[9] J. Tersoff and D. R. Hamann, Phys. Rev. B **31**, 805 (1985).
[10] R. M. Tromp, E. J. van Loenen, J. E. Demuth, and N. D. Lang, Phys. Rev. B **37**, 9042 (1988).
[11] J. Wintterlin, J. Wiechers, H. Brune, T. Gritsch, H. Hofer, and R. J. Behm, Phys. Rev. Lett. **62**, 59 (1989).
[12] N. J. Zheng and I. S. T. Tsong, Phys. Rev. B **41**, 2671 (1990).
[13] W. A. Hofer, A. Garcia-Lekue, and H. Brune, Chem. Phys. Lett. **397**, 354 (2004).
[14] W. A. Hofer, Prog. Surf. Sci. **71**, 147 (2003).
[15] W. A. Hofer, A. S. Foster, and A. L. Shluger, Rev. Mod. Phys. **75**, 1287 (2003).
[16] J. E. Demuth, U. Kohler, and R. J. Hamers, J. Microsc. **152**, 299 (1988).
[17] V. M. Hallmark, S. Chiang, J. F. Rabolt, J. D. Swalen, and R. J. Wilson, Phys. Rev. Lett. **59**, 2879 (1987).
[18] C. J. Chen, Phys. Rev. Lett. **65**, 448 (1990).
[19] C. J. Chen, Phys. Rev. B **42**, 8841 (1990).
[20] C. J. Chen, Phys. Rev. Lett. **69**, 1656 (1992).
[21] W. Sacks, Phys. Rev. B **61**, 7656 (2000).
[22] L. Jurczyszyn, N. Mingo, and F. Flores, Surf. Sci. **402-404**, 459 (1998).
[23] F. Calleja, A. Arnau, J. J. Hinarejos, A. L. Vázquez de Parga, W.

A. Hofer, P. M. Echenique, and R. Miranda, Phys. Rev. Lett. **92**, 206101 (2004).
[24] C. Corriol, F. Calleja, A. Arnau, J. J. Hinarejos, A. L. Vázquez de Parga, W. A. Hofer, and R. Miranda, Chem. Phys. Lett. **405**, 131 (2005).
[25] P. Mallet, W. Sacks, D. Roditchev, D. Defourneau, and J. Klein, J. Vac. Sci. Technol. B **14**, 1070 (1996).
[26] F. J. Giessibl, S. Hembacher, H. Bielefeldt, and J. Mannhart, Science **289**, 422 (2000).
[27] S. Hembacher, F. J. Giessibl, and J. Mannhart, Science **305**, 380 (2004).
[28] F. Giessibl, Mater. Today **8**, 32 (2005).
[29] L. A. Zotti, W. A. Hofer, and F. J. Giessibl, Chem. Phys. Lett. **420**, 177 (2006).
[30] M. Herz, F. J. Giessibl, and J. Mannhart, Phys. Rev. B **68**, 045301 (2003).
[31] V. F. Gantmakher, V. A. Gasparov, G. I. Kulesko, and V. N. Matveev, Zh. Eksp. Teor. Fiz. **63**, 1752 (1972) [Sov. Phys. JETP **36**, 925 (1973)].
[32] M. Wuttig, R. Franchy, and H. Ibach, Surf. Sci. **213**, 103 (1989).
[33] S. Murphy, G. Manai, and I. V. Shvets, Surf. Sci. **579**, 65 (2005).
[34] D. A. Walko and I. K. Robinson, Surf. Rev. Lett. **6**, 851 (1999).
[35] E. Vileg, S. M. Driver, P. Goedtkindt, P. J. Knight, W. Liu, J. Ludecke, K. A. R. Mitchell, V. Murashov, I. K. Robinson, S. A. de Vries, and D. P. Woodruff, Surf. Sci. **516**, 16 (2002).
[36] A. R. H. Clarke, J. B. Pethica, J. A. Nieminen, F. Besenbacher, E. Laegsgaard, and I. Stensgaard, Phys. Rev. Lett. **76**, 1276 (1996).
[37] A. N. Chaika, V. N. Semenov, S. S. Nazin, S. I. Bozhko, S. Murphy, K. Radican, and I. V. Shvets, Phys. Rev. Lett. **98**, 206101 (2007).
[38] I. Horcas, R. Fernandez, J. M. Gomez-Rodriguez, J. Colchero, J. Gomez-Herrero, and A. M. Baro, Rev. Sci. Instrum. **78**, 013705 (2007).
[39] D. A. Papaconstantopoulos, *Handbook of the Band Structure of Elemental Solids* (Plenum, New York, 1986).
[40] D. Sekiba, T. Inokuchi, Y. Wakimoto, K. Yagi-Watanabe, and H. Fukitani, Surf. Sci. **470**, 43 (2000).
[41] J. S. Kasper and J. S. Kouvel, J. Phys. Chem. Solids **11**, 231 (1959).
[42] L. Pál, E. Krén, G. Kádár, P. Szabó, and T. Tarnóczi, J. Appl. Phys. **39**, 538 (1968).
[43] W. Harrison, *Electronic Structure and the Properties of Solids* (Freeman, San Francisco, 1980).
[44] A. L. Vázquez de Parga, O. S. Hernán, R. Miranda, A. Levy Yeyati, N. Mingo, A. Martín-Rodero, and F. Flores, Phys. Rev. Lett. **80**, 357 (1998).
[45] M. D. Segall, P. J. D. Lindan, M. J. Probert, C. J. Pickard, P. J. Hasnip, S. J. Clark, and M. C. Payne, J. Phys.: Condens. Matter **14**, 2717 (2002).
[46] J. P. Perdew, J. A. Chevary, S. H. Vosko, K. A. Jackson, M. R. Pederson, D. J. Singh, and C. Fiolhais, Phys. Rev. B **46**, 6671 (1992).
[47] D. Vanderbilt, Phys. Rev. B **41**, 7892 (1990).
[48] A. Sakuma, J. Magn. Magn. Mater. **187**, 105 (1998).
[49] B. G. Pfrommer, M. Cote, S. G. Louie, and M. L. Cohen, J. Comput. Phys. **131**, 133 (1997).
[50] M. R. Sørensen, K. W. Jacobsen, and H. Jónsson, Phys. Rev. Lett. **77**, 5067 (1996).
[51] H.-J. Guntherodt and R. Wiesendanger, *Scanning Tunnelling Microscopy I* (Springer-Verlag, Berlin, 1991).